A multiple level set method for three-dimensional inversion of magnetic data

Wenbin Li * Wangtao Lu † Jianliang Qian ‡

July 26, 2015

Abstract

We propose a multiple level set method for inverting three-dimensional magnetic data induced by magnetization only. To alleviate inherent non-uniqueness of the inverse magnetic problem, we assume that the subsurface geological structure consists of several uniform magnetic mass distributions surrounded by homogeneous non-magnetic background such as soil, where each magnetic mass distribution has a known constant susceptibility and is supported on an unknown sub-domain. This assumption enables us to reformulate the original inverse magnetic problem into a domain inverse problem for those unknown domains defining the supports of those magnetic mass distributions. Since each uniform mass distribution may take a variety of shapes, we use multiple level-set functions to parameterize these domains so that the domain inverse problem can be further reduced to an optimization problem for multiple level-set functions. To compute rapidly gradients of the nonlinear functional arising in the multiple-level-set formulation, we utilize the fact that the kernel function in the field-susceptibility relation decays rapidly off the diagonal so that matrix-vector multiplications for evaluating the gradients can be speeded up significantly. Numerical experiments are carried out to illustrate the effectiveness of the new method.

1 Introduction

In exploration geophysics, one challenging problem is to interpret a great amount of three-dimensional (3-D) magnetic survey data measured on some surface of the earth in order to

*Department of Mathematics, Michigan State University, East Lansing, MI 48824, USA. Email: **wenbinli@math.msu.edu**

†Department of Mathematics, Michigan State University, East Lansing, MI 48824, USA. Email: **wangtaol@math.msu.edu**

‡Department of Mathematics, Michigan State University, East Lansing, MI 48824, USA. Email: **qian@math.msu.edu**

map subsurface geological structure. Robust and efficient inversion methods for magnetic anomalous data are called for when detailed survey is required in practice. Mathematically, it is well-known that there exist infinitely many subsurface structures that reproduce magnetic data within the same level of accuracy so that the solution for the magnetic inverse problem is theoretically non-unique. To overcome this difficulty, a prior information is usually incorporated in the inversion process so that a geologically reasonable model can be selected in the family of mathematically acceptable models.

Existing methods for dealing with such non-uniqueness of the inverse problem can be categorized into two approaches according to [21]. The first approach is based on parametric inversion, where geometric parameters of the model are fixed so that magnetic susceptibilities within the given geometry are sought in a nonlinear inversion [2, 38]. Since only a small subset of possible solutions is involved in the inversion, non-uniqueness is not generally an issue due to the restrictive nature of the inversion algorithm.

The second approach is to divide the earth into a large number of cells with fixed sizes and unknown constant susceptibilities, and those in-cell susceptibilities are sought in the inversion; two representative works using such an approach are [21, 28]. In such an approach, in-cell susceptibilities are obtained by minimizing an objective functional, generally consisting of a misfit functional and a stabilizing functional (a.k.a the regularization term), to fit the data. In principle, Tikhonov regularization theory can guarantee the uniqueness of the solution. To ensure that the solution is geologically reasonable, a priori information is required in the formulation.

In [21], the authors utilized in their stabilizing functional a so-called depth-weighting function, which was chosen empirically according to a priori information, so that the resulting model can capture correct depth of the causative body. The algorithm described in [28] also involved a weighting function that, in contrast to the aforementioned one, is independent of a priori information; however, this formulation requires a prior knowledge of the range of subsurface magnetic susceptibility so that further constraints can be imposed to improve the geological feasibility of the final solution. As pointed out in [6, 10], the weighting function can affect the robustness of the inversion method since the best weighting function should be chosen based on the geometry of causative body, which is difficult to obtain in practice. Moreover, since most inversion techniques provide quantitative descriptions for geological structures, one has to extract the position of causative body from resulting models afterwards, and this is not an easy task. Therefore, we are motivated to develop a method, which does not rely on weighting functions and can directly delineate causative bodies beneath the surface.

We propose a multiple level set method for inverting 3-D magnetic anomalous data which are induced by magnetization only, and this method automatically determines positions of causative bodies and does not involve any weighting function. The method is an extension of recently developed single level set methods for the inversion of gravity and gravity gradient data [13, 14, 24, 25]. Mathematically, we formulate the inversion of magnetic anomalous data as the following inverse problem: recover the magnetic susceptibility distribution χ in

a subsurface domain Ω, from the data d measured on a measurement surface $\Gamma \in \mathbf{R}^3/\Omega$. To alleviate the non-uniqueness of the inverse magnetic problem, we assume that the subsurface geological structure in domain Ω consists of n uniform magnetic mass distributions surrounded by a homogeneous non-magnetic background such as soil, where each magnetic mass distribution has a known constant susceptibility and is supported on an unknown subdomain so that the susceptibility contrast relative to the non-magnetic background satisfies

$$\chi(\mathbf{r}) = 0, \quad \mathbf{r} \in \Omega_0; \quad \chi(\mathbf{r}) = \chi_i, \quad \mathbf{r} \in D_i; \quad \Omega_0 \cup (\cup_i D_i) = \Omega; \quad D_i \cap D_j = \emptyset, \tag{1}$$

where Ω_0 is the background domain, and D_i is the support of the i-th homogeneous material with susceptibility contrast χ_i. Such an assumption is reasonable due to the following reason: although χ is generally not piecewise constant in practice, by the equivalent source principle, one can always find an averaged susceptibility χ_i along with an average domain D_i for each causative body in Ω so that χ defined in equation (1) can reproduce the same magnetic data; in fact, there can exist infinitely many such models $\{\chi_i, D_i\}_{i=1}^n$. Usually, a prior information about the model under consideration can help determine $\{\chi_i\}_{i=1}^n$ so that only $\{D_i\}_{i=1}^n$ need to be sought. Consequently, we convert the original inverse problem into a domain inverse problem.

Since each unknown domain D_i may take a variety of possible shapes, connected or disconnected, we may introduce multiple level set functions to parametrize all n domains D_i [8] so that the domain inverse problem is reduced to a nonlinear optimization problem for multiple level set functions; such multiple level set formulation becomes essential when there are more than two different homogeneous mediums in Ω. To compute rapidly the gradient of the nonlinear functional with respect to each of the multiple level set functions, we make use of the fact that the kernel function in the relation between field data $\mathbf{d}$ and the susceptibility χ decays rapidly off the diagonal so that matrix-vector multiplications for evaluating the gradients can be speeded up significantly.

The reason that we choose the level-set method for the inverse magnetic problem is the following. For the geometrical domain inverse problem under consideration, one needs to deal with closed irregular surfaces which are the boundary of an underlying domain. To describe such an irregular surface, one may introduce some surface parametrization so that one can carry out manipulation on such a surface in order to fit the given data. However, because such an irregular surface may change shapes or connectivities during nonlinear data-fitting process, we need to design a reliable and robust parameterization which is capable of changing shapes or connectivities automatically, and the level-set implicit parametrization [26] is exactly such a parametrization. We start with a continuous function which is defined everywhere in the whole computational domain, and we further require that this function be positive inside a targeted domain and negative outside, which implies that the zero level-set where the function is zero describes exactly the boundary of the targeted domain, and this function is called the level-set function. A level-set implicit parametrization gives rise to many advantages, such as we have a globally defined functions to manipulate, and the changes of geometry shape and connectivities can be automatically taken care of due to the

underlying physical mechanism.

We remark that in the literature the level-set method [26] has been widely used as a suitable and powerful tool for interfaces and shape-optimization problems mainly due to its ability in automatic interface merging and topological changes. In terms of non-geophysical inverse problems, the level-set method was first used for inverse obstacle problems in [34]; since then it has been applied to a variety of inverse problems. In [23] it was used to reconstruct 2-D binary obstacles; in [4] different choices of descent directions to evolve level-sets were proposed for inverse obstacle problems; furthermore, the level-set method was used for inverse scattering problems to reconstruct geometry of extended targets in [11] and [9], for electrical impedance tomography and electrical resistance tomography in medical imaging in [7, 1], and for piece-wise constant surface reconstruction in [37]. In terms of geophysical inverse problems, the level-set method has also found its wide applications, and the following citations are by no means complete. In [13], the level-set method was first applied to the gravity data; in [27] it was applied to identify uncertainties in the shape of geophysical objects using temperature measurements; in [41], [19] and [20] it was applied to travel-time tomography problems in different settings.

The rest of this paper is organized as follows. In section 2, we present the forward model of magnetic data. In section 3, we develop the multiple level-set based inversion of 3-D magnetic data. In section 4, we present the key algorithm of the magnetic inversion along with some implementation details. In section 5, intensive numerical examples are studied to illustrate the effectiveness of our level-set algorithm; in addition, the issue of inherent non-uniqueness is addressed and discussed. Finally, we draw our conclusion.

2 Forward model of magnetic data

We work with the anomalous magnetic flux arising from subsurface susceptible magnetic mass distributions. Supposing that there is no remanent magnetization and the demagnetization effect is negligible in comparison to the primary inducing magnetic field, and the data are acquired in free space (e.g. air), the linear model of magnetic anomaly data is given by the following equation [16, 40]:

$$\mathbf{B}(\mathbf{r}) = \frac{1}{4\pi}\nabla_{\mathbf{r}} \int_{\Omega} \chi(\tilde{\mathbf{r}})\mathbf{B}^0 \cdot \nabla_{\mathbf{r}} \left(\frac{1}{|\mathbf{r}-\tilde{\mathbf{r}}|} \right) \mathrm{d}\tilde{\mathbf{r}}, \quad \mathbf{r} \in \Gamma. \tag{2}$$

In equation (2), $\mathbf{B}(\mathbf{r})$ is the anomalous magnetic flux observed above the subsurface, and $\mathbf{B}^0$ is a constant vector which denotes the magnetic flux of the primary inducing field; both $\mathbf{B}(\mathbf{r})$ and $\mathbf{B}^0$ have the units of Tesla (T) or nanotesla (nT). $\chi(\tilde{\mathbf{r}})$ is the magnetic susceptibility in the rock formations, which is dimensionless in the SI system. $\Omega \subset \mathbf{R}^3$ is a subsurface domain and $\Gamma \subset \mathbf{R}^3 \setminus \Omega$ is the measurement surface. $\mathbf{r}$ and $\tilde{\mathbf{r}}$ denote spatial coordinates. The notation $\nabla_{\mathbf{r}}$ means the gradient with respect to the spatial coordinate $\mathbf{r}$, and $|\cdot|$ denotes the vector l^2-norm.

We can express $\mathbf{B}^0$ as $\mathbf{B}^0 = B^0\mathbf{l}$, where B^0 denotes the strength of the primary inducing field and $\mathbf{l}$ denotes the corresponding direction. Plugging this expression into equation (2) and evaluating $\nabla_{\mathbf{r}}$ explicitly in the 3-D space yields an equivalent equation for the anomalous flux

$$\mathbf{B}(\mathbf{r}) = \frac{1}{4\pi} B^0 \int_\Omega \chi(\tilde{\mathbf{r}}) \frac{1}{|\mathbf{r}-\tilde{\mathbf{r}}|^3} \left[\frac{3\left(\mathbf{l}\cdot(\mathbf{r}-\tilde{\mathbf{r}})\right)(\mathbf{r}-\tilde{\mathbf{r}})}{|\mathbf{r}-\tilde{\mathbf{r}}|^2} - \mathbf{l} \right] \mathrm{d}\tilde{\mathbf{r}}.$$

Moreover, measurements in geophysical magnetic surveys are usually taken along the total magnetic field which can be computed approximately as [40]:

$$\begin{aligned} d(\mathbf{r}) &\equiv \mathbf{l}\cdot\mathbf{B}(\mathbf{r}) \\ &= \frac{1}{4\pi} B^0 \int_\Omega \chi(\tilde{\mathbf{r}}) \frac{1}{|\mathbf{r}-\tilde{\mathbf{r}}|^3} \left[\frac{3\left(\mathbf{l}\cdot(\mathbf{r}-\tilde{\mathbf{r}})\right)^2}{|\mathbf{r}-\tilde{\mathbf{r}}|^2} - 1 \right] \mathrm{d}\tilde{\mathbf{r}}, \quad \mathbf{r}\in\Gamma. \end{aligned} \tag{3}$$

In this paper we use equation (3) as the forward model of magnetic anomaly data induced by magnetization only. The purpose of magnetic survey is to recover the susceptibility distribution $\chi(\tilde{\mathbf{r}})$ from the measurement data $d(\mathbf{r})$ which is observed above the subsurface.

3 Magnetic inversion and the level set formulation

In this section we develop the method for 3-D inversion of magnetic data, where a continuous formulation based on equation (3) is adopted in the derivation. We propose a level set framework for the reconstruction of susceptibility distributions.

3.1 Data fitting

Denoting the observed survey data of anomalous magnetic flux by d^*, and supposing that d is the predicted data from the forward model in equation (3), we propose the misfit function for data fitting as the following,

$$E_d = \frac{1}{2}\int_\Gamma (d-d^*)^2 \, \mathrm{d}\mathbf{r}. \tag{4}$$

This is a commonly used objective function in magnetic inversion [21, 15, 25], and the model parameter (i.e. the susceptibility distribution) χ is recovered by minimizing this misfit function E_d.

We study the Fréchet derivative of E_d by considering a perturbation on the predicted data d: $d \to d + \delta d$, which leads to the corresponding perturbation on E_d:

$$\delta E_d = \int_\Gamma (d-d^*)\cdot\delta d \, \mathrm{d}\mathbf{r}. \tag{5}$$

The predicted data $d(\mathrm{r})$ are related to the model parameter $\chi(\tilde{\mathbf{r}})$ by equation (3) so that we have

$$\delta d = \frac{1}{4\pi} B^0 \int_\Omega \delta\chi(\tilde{\mathbf{r}}) \cdot K(\mathbf{r}, \tilde{\mathbf{r}})\, \mathrm{d}\tilde{\mathbf{r}} \tag{6}$$

where $K(\mathbf{r}, \tilde{\mathbf{r}})$ denotes the integral kernel:

$$K(\mathbf{r}, \tilde{\mathbf{r}}) = \frac{1}{|\mathbf{r} - \tilde{\mathbf{r}}|^3} \left[\frac{3\left(\mathbf{l} \cdot (\mathbf{r} - \tilde{\mathbf{r}})\right)^2}{|\mathbf{r} - \tilde{\mathbf{r}}|^2} - 1 \right], \quad \mathbf{r} \in \Gamma,\ \tilde{\mathbf{r}} \in \Omega. \tag{7}$$

Substituting equation (6) into equation (5), we get the equation relating δE_d to $\delta\chi$,

$$\delta E_d = \frac{1}{4\pi} B^0 \int_\Omega \delta\chi(\tilde{\mathbf{r}}) \cdot \left[\int_\Gamma (d(\mathbf{r}) - d^*(\mathbf{r})) \cdot K(\mathbf{r}, \tilde{\mathbf{r}}) \mathrm{d}\mathbf{r} \right] \mathrm{d}\tilde{\mathbf{r}},$$

so that the Fréchet derivative of E_d with respect to $\chi(\tilde{\mathbf{r}})$ is obtained as the following

$$\frac{\partial E_d}{\partial \chi} = \frac{1}{4\pi} B^0 \int_\Gamma (d(\mathbf{r}) - d^*(\mathbf{r})) \cdot K(\mathbf{r}, \tilde{\mathbf{r}})\, \mathrm{d}\mathbf{r}. \tag{8}$$

A necessary condition for minimizing E_d is that the Fréchet derivative $\partial E_d / \partial \chi$ equals zero.

3.2 Level set formulations for susceptibility distribution

A principal difficulty with the inversion of magnetic data (and other geopotential data) is the inherent non-uniqueness [21, 22]. By Gauss's theorem, if the field distribution is known only on a bounding surface, there are infinitely many equivalent source distributions inside the boundary that can produce the known field.

To alleviate the inherent non-uniqueness, we assume that the subsurface geological structure in domain Ω consists of n uniform magnetic mass distributions surrounded by a homogeneous non-magnetic background such as soil, where each magnetic mass distribution has a known constant susceptibility and is supported on an unknown sub-domain so that the susceptibility contrast relative to the non-magnetic background satisfies

$$\chi(\tilde{\mathbf{r}}) = 0, \quad \tilde{\mathbf{r}} \in \Omega_0; \quad \chi(\tilde{\mathbf{r}}) = \chi_i, \quad \tilde{\mathbf{r}} \in D_i; \quad \Omega_0 \cup (\cup_i D_i) = \Omega; \quad D_i \cap D_j = \emptyset, \tag{9}$$

where Ω_0 is the background domain, and D_i is the support of the i-th homogeneous material with susceptibility contrast χ_i. We suppose that the values of χ_i's are known due to some a priori knowledge in the types of underlying minerals. Moreover the domain D_i is not necessarily connected, which means that an identical mineral can be distributed separately in the subsurface. In this paper we adopt the level set method [26] to describe the domain-wise homogeneous distribution of susceptibility. We use a single level set method to handle the case with one type of primary mineral in the subsurface, and we propose a multiple level set method [8] to deal with the case with two types of primary minerals. The methodology can be generalized to the domain-wise homogeneous structure with arbitrarily many types of compositions, but the inherent non-uniqueness in the magnetic inversion problem prevents us to do so for more than three types of primary minerals.

3.2.1 Single level-set formulation

To start with, we assume that there is only one type of magnetic mineral in the subsurface structure, and the average susceptibility of the mineral is known as χ_0. Therefore the susceptibility distribution is given by

$$\chi(\tilde{\mathbf{r}}) = \chi_0,\ \tilde{\mathbf{r}} \in D_0; \quad \chi(\tilde{\mathbf{r}}) = 0,\ \tilde{\mathbf{r}} \in \Omega \setminus D_0.$$

We use a level set formulation to express this distribution:

$$\chi(\tilde{\mathbf{r}}) = \chi_0 \cdot H(\phi_0(\tilde{\mathbf{r}})), \tag{10}$$

where $\phi_0(\tilde{\mathbf{r}})$ is the level set function

$$\phi_0(\tilde{\mathbf{r}}) = \begin{cases} > 0 & , \quad \tilde{\mathbf{r}} \in D_0 \\ < 0 & , \quad \tilde{\mathbf{r}} \in \Omega \setminus D_0 \end{cases}$$

and $H(x)$ is the heaviside function

$$H(x) = \begin{cases} 1 & , \quad x \geq 0 \\ 0 & , \quad x < 0 \end{cases}. \tag{11}$$

The level set function $\phi_0(\tilde{\mathbf{r}})$ parameterizes the unknown domain D_0, and the susceptibility distribution $\chi(\tilde{\mathbf{r}})$ is reconstructed by recovering $\phi_0(\tilde{\mathbf{r}})$.

From equation (10) one can get

$$\frac{\partial \chi}{\partial \phi_0} = \chi_0 \cdot H'(\phi_0) = \chi_0 \cdot \delta_d(\phi_0), \tag{12}$$

where $\delta_d(\phi_0)$ is the Dirac delta function [3]. Combining equation (12) and equation (8), one gets the Fréchet derivative of the misfit function E_d with respect to the level set function ϕ_0:

$$\frac{\partial E_d}{\partial \phi_0} = \frac{\partial E_d}{\partial \chi} \cdot \frac{\partial \chi}{\partial \phi_0} = \frac{1}{4\pi} \chi_0 B^0 \cdot \delta_d(\phi_0) \int_\Gamma \left(d(\mathbf{r}) - d^*(\mathbf{r})\right) K(\mathbf{r}, \tilde{\mathbf{r}})\, \mathrm{d}\mathbf{r}. \tag{13}$$

Equation (13) relates the objective function to the new model parameter ϕ_0, and a necessary condition for minimizing E_d is $\partial E_d / \partial \phi_0 = 0$.

3.2.2 Multiple level-set formulation

For the case with two types of magnetic minerals in the subsurface, we are looking for a domain-wise homogeneous distribution of susceptibility with multiple compositions:

$$\chi(\tilde{\mathbf{r}}) = \begin{cases} \chi_1 & , \quad \tilde{\mathbf{r}} \in D_1 \\ \chi_2 & , \quad \tilde{\mathbf{r}} \in D_2 \\ 0 & , \quad \tilde{\mathbf{r}} \in \Omega \setminus (D_1 \cup D_2) \end{cases}, \tag{14}$$

where χ_1 and χ_2 are average susceptibilities of the minerals in D_1 and D_2 respectively. Supposing that the values of χ_1 and χ_2 are known, we use a multiple level set formulation [8] to express the magnetic susceptibility:

$$\chi(\tilde{\mathbf{r}}) = \chi_1 \cdot H(\phi_1)\,(1 - H(\phi_2)) + \chi_2 \cdot (1 - H(\phi_1))\,H(\phi_2). \tag{15}$$

In formula (15), ϕ_i is the level set function for D_i $(i = 1, 2)$,

$$\phi_i(\tilde{\mathbf{r}}) = \begin{cases} > 0 & , \quad \tilde{\mathbf{r}} \in D_i \\ < 0 & , \quad \tilde{\mathbf{r}} \in \Omega \setminus D_i \end{cases}$$

and $H(x)$ is the heaviside function given in equation (11). Equation (15) is a robust formulation for the distribution of susceptibility in equation (14). In the inversion process there may exist the region $E = \{\tilde{\mathbf{r}} \mid \phi_1(\tilde{\mathbf{r}}) > 0,\ \phi_2(\tilde{\mathbf{r}}) > 0\}$, and equation (15) gives $\chi(\tilde{\mathbf{r}}) = 0$ in such a region and avoids the artificial value $\chi(\tilde{\mathbf{r}}) = \chi_1 + \chi_2$ which may be generated by a trivial level set formulation such as $\chi(\tilde{\mathbf{r}}) = \chi_1 \cdot H(\phi_1) + \chi_2 \cdot H(\phi_2)$. Moreover, formulation (15) can be simply generalized to handle a domain-wise homogeneous structure with more compositions [36, 8].

From equation (15) one can compute the Fréchet derivatives of $\chi(\tilde{\mathbf{r}})$ with respect to the new model parameters ϕ_1 and ϕ_2,

$$\frac{\partial \chi}{\partial \phi_1} = \delta_d(\phi_1) \cdot (\chi_1 - (\chi_1 + \chi_2)H(\phi_2))\,, \tag{16}$$

$$\frac{\partial \chi}{\partial \phi_2} = \delta_d(\phi_2) \cdot (\chi_2 - (\chi_1 + \chi_2)H(\phi_1))\,, \tag{17}$$

where $\delta_d(\cdot)$ denotes the Dirac delta function. Combining equations (16) and (17) with equation (8), one gets the Fréchet derivatives of the misfit function E_d with respect to ϕ_1 and ϕ_2,

$$\frac{\partial E_d}{\partial \phi_1} = \frac{1}{4\pi}\delta_d(\phi_1) \cdot (\chi_1 - (\chi_1 + \chi_2)H(\phi_2)) \cdot B^0 \int_\Gamma (d(\mathbf{r}) - d^*(\mathbf{r}))\,K(\mathbf{r}, \tilde{\mathbf{r}})\,\mathrm{d}\mathbf{r}, \tag{18}$$

$$\frac{\partial E_d}{\partial \phi_2} = \frac{1}{4\pi}\delta_d(\phi_2) \cdot (\chi_2 - (\chi_1 + \chi_2)H(\phi_1)) \cdot B^0 \int_\Gamma (d(\mathbf{r}) - d^*(\mathbf{r}))\,K(\mathbf{r}, \tilde{\mathbf{r}})\,\mathrm{d}\mathbf{r}. \tag{19}$$

The necessary conditions for minimizing E_d are $\partial E_d/\partial \phi_i = 0$, $(i = 1, 2)$, and the susceptibility $\chi(\tilde{\mathbf{r}})$ is recovered by using the new model parameters ϕ_1 and ϕ_2.

3.3 Additional regularization

To make the update smooth in evolving the gradient descent flow, we introduce an additional regularization term into the objective function, and this regularization amounts to adding an

artificial viscosity term to stabilize the Hamilton-Jacobi based gradient flow. For the single level set formulation the regularization term is defined as

$$E_r = \frac{1}{2}\int_\Omega |\nabla\phi_0|^2 \, \mathrm{d}\tilde{\mathbf{r}},$$

and the total objective function is formed by the linear combination of E_d and E_r:

$$E_t = E_d + \alpha \cdot E_r \tag{20}$$

where E_d is the misfit function given in equation (4), and α is a small constant that indicates the amount of regularization one needs. The inversion algorithm is to minimize the new objective function E_t. The regularization term E_r tends to smoothen the shape of structure characterized by the zero level set $\{\tilde{\mathbf{r}} \mid \phi_0(\tilde{\mathbf{r}}) = 0\}$.

The Fréchet derivative of E_r is

$$\frac{\partial E_r}{\partial \phi_0} = -\Delta\phi_0$$

so that

$$\frac{\partial E_t}{\partial \phi_0} = \frac{\partial E_d}{\partial \phi_0} - \alpha\Delta\phi_0 \tag{21}$$

where $\frac{\partial E_d}{\partial \phi_0}$ is given by equation (13).

Since there are two level set functions for the multiple level set formulation (equation (15)), the regularization term is defined as

$$E_r = \frac{1}{2}\int_\Omega |\nabla\phi_1|^2 \, \mathrm{d}\tilde{\mathbf{r}} + \frac{1}{2}\int_\Omega |\nabla\phi_2|^2 \, \mathrm{d}\tilde{\mathbf{r}}.$$

Since the total objective function E_t is still in the form of equation (20), we have

$$\frac{\partial E_t}{\partial \phi_i} = \frac{\partial E_d}{\partial \phi_i} - \alpha\Delta\phi_i, \quad i = 1, 2 \tag{22}$$

where $\frac{\partial E_d}{\partial \phi_i}$ $(i = 1, 2)$ are evaluated in equations (18) and (19), respectively. The Fréchet derivatives $\frac{\partial E_t}{\partial \phi_i}$ illustrate the gradient descent directions of the total objective function.

3.4 Gradient descent method for minimization

We are looking for the model parameters ϕ_i which minimize the total objective function E_t, where $i = 0$ for the single level set formulation and $i = 1, 2$ for the multiple level set formulation. We use a gradient descent method for minimization so that we evolve the following gradient flow to the steady state to compute the minimizer,

$$\begin{aligned} \frac{\partial \phi_i}{\partial t} &= -\frac{\partial E_t}{\partial \phi_i} \qquad \text{in } \Omega \\ \frac{\partial \phi_i}{\partial \mathbf{n}} &= 0 \qquad \text{on } \partial\Omega \end{aligned} \tag{23}$$

where $\phi_i = \phi_i(\tilde{\mathbf{r}}, t)$ with t being the artificial evolution time, and a natural boundary condition for ϕ_i is imposed on the boundary $\partial\Omega$. The gradient directions $\frac{\partial E_t}{\partial \phi_i}$ are computed in subsection 3.3.

3.5 When magnetic inversion has a unique solution?

In domain problems of volume potential for inverse gravimetry, we have the following uniqueness result [12]: if the mass density is given as a constant on the underlying domain and the domain is star-shaped with respect to its center of gravity or is convex in a certain coordinate direction, then the exterior potential uniquely determines the underlying domain. Starting from this result, the works in [13, 14, 25, 24] developed various level-set methods to recover underlying source domains from measured exterior-potential related quantities. Assuming that the uniqueness condition holds, the level-set methods recover the underlying structure uniquely in those settings.

In domain inverse problems for magnetic data considered here, we do not have such uniqueness results yet. However, according to our numerical experiments, we have the following conjecture.

Conjecture. If the susceptibility distribution is given by a single characteristic function for a certain underlying domain, and the domain is star-shaped with respect to its center of gravity or is convex in a certain coordinate direction, then the total magnetic field uniquely determines the underlying domain.

Our single level-set formulation for magnetic data strongly indicates that this conjecture holds true. Proving this conjecture is an ongoing project.

4 Algorithm and numerical implementation

4.1 Algorithm sketch

In this section, we summarize the above-mentioned algorithm on magnetic inversion and describe the numerical implementation in details.

Algorithm: multiple level set method for 3-D magnetic inversion

1. Initialization. Initialize the level set functions ϕ_i, where $i = 0$ in the single level set formulation and $i = 1, 2$ in the multiple level set formulation.

2. Obtain the magnetic susceptibility $\chi(\tilde{\mathbf{r}})$ according to equation (10) or equation (15).

3. Compute the predicted data $d(\mathbf{r})$ along the measurement surface Γ according to equation (3).

4. Compute the gradient directions of the total objective function E_t. For the single level set formulation $\frac{\partial E_t}{\partial \phi_0}$ is given by equation (21), and for the multiple level set formulation $\frac{\partial E_t}{\partial \phi_i}$ $(i = 1, 2)$ are given by equation (22).

5. Evolve the level set functions ϕ_i according to the gradient flow (23).

6. Reinitialize the level set functions to maintain the signed distance property.

7. Go back to step 2 until the iteration converges.

In step 2, the Heaviside function $H(\phi)$ in the level set formulation is numerically approximated by

$$H_\epsilon(\phi) = \begin{cases} 0 & , \quad \phi < -\epsilon \\ \frac{1}{2} + \frac{\phi}{2\epsilon} + \frac{1}{2\pi} \sin\left(\frac{\pi\phi}{\epsilon}\right) & , \quad -\epsilon \le \phi \le \epsilon \\ 1 & , \quad \epsilon < \phi \end{cases}$$

In step 4, the Dirac delta function $\delta_d(\phi_i)$ appearing in the gradient directions $\frac{\partial E_t}{\partial \phi_i}$ is numerically approximated by $(\delta_d)_\epsilon(\phi_i) = \mathcal{I}_{T_\epsilon^i} \cdot |\nabla \phi_i|$ [39, 25], where

$$\mathcal{I}_{T_\epsilon^i} = \begin{cases} 1 & , \quad \tilde{\mathbf{r}} \in T_\epsilon^i \\ 0 & , \quad \tilde{\mathbf{r}} \in \Omega \setminus T_\epsilon^i \end{cases} \tag{24}$$

with support $T_\epsilon^i = \{\tilde{\mathbf{r}} \in \Omega : \ |\phi_i(\tilde{\mathbf{r}})| \le \epsilon\}$. Then the gradient directions $\frac{\partial E_t}{\partial \phi_i}$ in (21) and (22) are evaluated by the following formulas,

$$\frac{\partial E_t}{\partial \phi_i} = F_i \cdot |\nabla \phi_i| - \alpha \Delta \phi_i$$

where $i = 0$ for the single level set formulation and $i = 1, 2$ for the multiple level set formulation. From equations (13), (18) and (19) one can find that

$$\begin{aligned} F_0 &= \frac{1}{4\pi} \chi_0 \cdot B^0 \cdot \mathcal{I}_{T_\epsilon^0} \int_\Gamma \left(d(\mathbf{r}) - d^*(\mathbf{r})\right) K(\mathbf{r}, \tilde{\mathbf{r}}) \, \mathrm{d}\mathbf{r}, \\ F_1 &= \frac{1}{4\pi} \left(\chi_1 - (\chi_1 + \chi_2) H_\epsilon(\phi_2)\right) \cdot B^0 \cdot \mathcal{I}_{T_\epsilon^1} \int_\Gamma \left(d(\mathbf{r}) - d^*(\mathbf{r})\right) K(\mathbf{r}, \tilde{\mathbf{r}}) \, \mathrm{d}\mathbf{r}, \\ F_2 &= \frac{1}{4\pi} \left(\chi_2 - (\chi_1 + \chi_2) H_\epsilon(\phi_1)\right) \cdot B^0 \cdot \mathcal{I}_{T_\epsilon^2} \int_\Gamma \left(d(\mathbf{r}) - d^*(\mathbf{r})\right) K(\mathbf{r}, \tilde{\mathbf{r}}) \, \mathrm{d}\mathbf{r}, \end{aligned}$$

where the predicted data $d(\mathbf{r})$ is computed in step 3 according to equation (3)

$$d(\mathbf{r}) = \frac{1}{4\pi} B^0 \int_\Omega \chi(\tilde{\mathbf{r}}) \cdot K(\mathbf{r}, \tilde{\mathbf{r}}) \, \mathrm{d}\tilde{\mathbf{r}}.$$

To evaluate the integrals in the above equations, we develop a low-rank-matrix decomposition algorithm to speed up matrix-vector multiplications arising in the numerical integrations. The detailed formulations are described below.

Then in step 5, the evolution equation (23) is reduced to the following form

$$\frac{\partial \phi_i}{\partial t}\left(= -\frac{\partial E_t}{\partial \phi_i}\right) = -F_i \cdot |\nabla \phi_i| + \alpha \Delta \phi_i,$$

which can be viewed as a Hamilton-Jacobi equation with an artificial viscosity term. We simply apply forward-difference in the time direction and central-difference for the spatial derivative. Related techniques have been widely used in the level set community in various applications [26, 32, 33, 29, 30, 18, 31, 5, 17]. Numerically there is a CFL condition to maintain the stability of evolution,

$$\Delta t \cdot \left(\frac{\max |F_i|}{\min\{\Delta x, \Delta y, \Delta z\}} + \frac{\alpha}{\min\{\Delta x^2, \Delta y^2, \Delta z^2\}}\right) < 1.$$

Since in our inversion algorithm the regularization weight α is much smaller than $\max |F_i|$, the CFL condition can be reduced as

$$\Delta t \cdot \left(\frac{\max |F_i|}{\min\{\Delta x, \Delta y, \Delta z\}}\right) < 1.$$

In practice, we take the time step

$$\Delta t = 0.5 \cdot \frac{\min\{\Delta x, \Delta y, \Delta z\}}{\max |F_0|}$$

in the single level set formulation, and

$$\Delta t = 0.5 \cdot \frac{\min\{\Delta x, \Delta y, \Delta z\}}{\max\{|F_1|, |F_2|\}}$$

in the multiple level set formulation.

In step 6, the level set reinitialization [35] is applied to maintain the signed distance property of ϕ_i. This is a standard technique in the level set method, and it can be viewed as a regularization on the model parameters ϕ_i [13, 19, 20]. Specifically, we solve the following system in an artificial time direction ξ

$$\begin{aligned} \frac{\partial \Phi_i}{\partial \xi} + \text{sign}(\phi_i) \cdot (|\nabla \Phi_i| - 1) &= 0, \\ \Phi_i(\tilde{\mathbf{r}}, \xi = 0) &= \phi_i(\tilde{\mathbf{r}}), \\ \left.\frac{\partial \Phi}{\partial \mathbf{n}}\right|_{\partial\Omega} &= 0, \end{aligned}$$

where $\text{sign}(\phi_i) = \frac{2}{\pi}\arctan\phi_i$ is the signum function [30, 19, 20]. Since the structure characterized by the level set function is mainly determined by the zero level set, in practice there is no need to get the steady state solution. In our numerical implementation we only evolve this equation for two $\Delta\xi$ steps and replace the original level set function ϕ_i with the solution Φ_i, where $i = 0$ in the single level set formulation and $i = 1, 2$ in the multiple level set formulation.

4.2 A low-rank-matrix decomposition algorithm for numerical integration

We develop a low-rank-matrix decomposition algorithm to evaluate the integrals arising in the magnetic-inversion problem. Without loss of generality, we provide the detailed formulations for the following two integrals:

$$P(\mathbf{r}) = \int_\Omega \chi(\tilde{\mathbf{r}}) \cdot K(\mathbf{r}, \tilde{\mathbf{r}})\, \mathrm{d}\tilde{\mathbf{r}}, \qquad \mathbf{r} \in \Gamma \tag{25}$$

$$F(\tilde{\mathbf{r}}) = \mathcal{I}_{T_\epsilon}(\tilde{\mathbf{r}}) \int_\Gamma (d(\mathbf{r}) - d^*(\mathbf{r}))\, K(\mathbf{r}, \tilde{\mathbf{r}})\, \mathrm{d}\mathbf{r}, \qquad \tilde{\mathbf{r}} \in \Omega \tag{26}$$

where $\mathcal{I}_{T_\epsilon}$ is given by equation (24), that

$$\mathcal{I}_{T_\epsilon}(\tilde{\mathbf{r}}) = \begin{cases} 1 & , \quad \tilde{\mathbf{r}} \in T_\epsilon \\ 0 & , \quad \tilde{\mathbf{r}} \in \Omega \setminus T_\epsilon \end{cases}$$

with support $T_\epsilon = \{\tilde{\mathbf{r}} \in \Omega : \ |\phi(\tilde{\mathbf{r}})| \le \epsilon\}$. The integral (25) arises in the computation of the predicted data $d(\mathbf{r})$; the integral (26) arises in the computation of gradient directions.

To describe the numerical integration, we take $\Omega = [0, X] \times [0, Y] \times [-Z, 0]$, which is uniformly discretized into $N = n_x \times n_y \times n_z$ points $\{\tilde{\mathbf{r}}_j\}_{j=1}^N$ with grid size $\tilde{h}$ in each direction. Then the measurement surface Γ is taken as $\Gamma = [0, X] \times [0, Y] \times \{z = \alpha, \alpha > 0\}$ and it is uniformly discretized into $M = m_x \times m_y$ points $\{\mathbf{r}_k\}_{k=1}^M$ with grid size h in each direction. Thus the integrals (25), (26) can be discretized as follows:

$$P(\mathbf{r}_k) \approx \tilde{h}^3 \cdot \sum_{j=1}^{N} \chi(\tilde{\mathbf{r}}_j)\, K(\mathbf{r}_k, \tilde{\mathbf{r}}_j), \qquad k = 1, 2, \cdots, M; \tag{27}$$

$$F(\tilde{\mathbf{r}}_j) \approx h^2 \cdot \mathcal{I}_{T_\epsilon}(\tilde{\mathbf{r}}_j) \sum_{k=1}^{M} (d(\mathbf{r}_k) - d^*(\mathbf{r}_k))\, K(\mathbf{r}_k, \tilde{\mathbf{r}}_j), \qquad j = 1, 2, \cdots, N. \tag{28}$$

Rewriting equations (27) and (28) in matrix form, we have

$$\mathbf{P} = \tilde{h}^3 \cdot \mathbf{K}\chi^T, \tag{29}$$

$$\mathbf{F} = h^2 \cdot \mathbf{d}^T\mathbf{K}\mathbf{D}, \tag{30}$$

where we have defined

$$\begin{aligned}
\mathbf{P} &= [P(\mathbf{r}_1), \cdots, P(\mathbf{r}_M)]^T, \\
\mathbf{d} &= [d(\mathbf{r}_1) - d^*(\mathbf{r}_1), \cdots, d(\mathbf{r}_M) - d^*(\mathbf{r}_M)]^T, \\
\chi &= [\chi(\tilde{\mathbf{r}}_1), \cdots, \chi(\tilde{\mathbf{r}}_N)], \\
\mathbf{F} &= [F(\tilde{\mathbf{r}}_1), \cdots, F(\tilde{\mathbf{r}}_N)],
\end{aligned}$$

and

$$\begin{aligned}
\mathbf{K} &= [K(\mathbf{r}_k, \tilde{\mathbf{r}}_j)]_{M\times N}, \\
\mathbf{D} &= \operatorname{diag}\{\mathcal{I}_{T_\epsilon}(\tilde{\mathbf{r}}_1), \cdots, \mathcal{I}_{T_\epsilon}(\tilde{\mathbf{r}}_N)\}.
\end{aligned}$$

Due to the large matrix $\mathbf{K} = [K(\mathbf{r}_k, \tilde{\mathbf{r}}_j)]_{M\times N}$, matrix-vector multiplications in equations (29) and (30) are of superlinear complexity

$$\mathcal{O}(MN) = \mathcal{O}(N^{5/3}),$$

and are expensive when N is large. Recalling that the integration kernel $K(\mathbf{r}_k, \tilde{\mathbf{r}}_j)$ is given by equation (7) and the magnitude of $K(\mathbf{r}_k, \tilde{\mathbf{r}}_j)$ decays rapidly when the distance $|\mathbf{r}_k - \tilde{\mathbf{r}}_j|$ increases, we are motivated to partition $\mathbf{K}$ into submatrices such that each submatrix is expected to have low-rank structure, based on which a fast algorithm can be developed to speed up relevant matrix-vector multiplications.

We first split the $N = n_x \times n_y \times n_z$ mesh points $\{\tilde{\mathbf{r}}_j\}_{j=1}^N$ into n_z sets

$$\{\tilde{\mathbf{r}}_l^i \mid 1 \le l \le \tilde{M}\}, \quad i = 1, \cdots, n_z,$$

with the z-coordinate of $\tilde{\mathbf{r}}_l^i$ being $-(i-1)\tilde{h}$, where $\tilde{M}$ denotes $n_x \times n_y$. According to this, we partition $\mathbf{K}$ into n_z submatrices $[\mathbf{K}^1, \mathbf{K}^2, \cdots, \mathbf{K}^{n_z}]$ where

$$\mathbf{K}^i = [K(\mathbf{r}_k, \tilde{\mathbf{r}}_l^i)]_{M\times\tilde{M}}.$$

To illustrate the partition more clearly, we provide a particular example. In our numerical implementation, the computational domain Ω is taken to be $\Omega = [0,1]\text{km}\times[0,1]\text{km}\times[-0.5,0]\text{km}$ and discretized into $N = 41 \times 41 \times 21 = 35301$ mesh points with grid size $\tilde{h} = 0.025$; the measurement surface Γ is set as $\Gamma = [0,1]\text{km} \times [0,1]\text{km} \times \{z = 0.1\text{km}\}$ and discretized into $M = 21 \times 21 = 441$ mesh grids with grid size $h = 0.05$. Thus the kernel matrix $\mathbf{K}$ is of size 441×35301, and it is partitioned into $n_z(= 21)$ 441×41^2 submatrices $[\mathbf{K}^1, \mathbf{K}^2, \cdots, \mathbf{K}^{21}]$, columns of which are indexed by mesh points with the z-coordinate $0, -0.025, -0.05, \cdots, -0.5$, respectively.

As Γ is parallel to the top of Ω, the distance between Γ and the slice $z = -(i-1)\tilde{h}$ increases as i increases so that entries in $\mathbf{K}^i$ decay rapidly with i increasing, and therefore the numerical rank of $\mathbf{K}^i$ decreases with i as well.

Next, we apply singular value decompositions (SVDs) to find a low-rank-matrix decomposition of $\mathbf{K}^i$ for $1 \le i \le n_z$. Starting with $\mathbf{K}^1$, we first compute its standard SVD:

$$\mathbf{K}^1 = \mathbf{U}^1 \mathbf{S}^1 (\mathbf{V}^1)^T,$$

where $\mathbf{U}^1$ is an $M \times M$ unitary matrix, $\mathbf{V}^1$ is an $\tilde{M} \times \tilde{M}$ unitary matrix, and $\mathbf{S}^1 = (\mathrm{diag}\{\sigma_s\})_{M \times \tilde{M}}$ is an $M \times \tilde{M}$ diagonal matrix with its diagonal entries being the singular values σ_s in descending order. Then we choose a threshold ϵ_{SVD}, set those singular values less than ϵ_{SVD} to be 0, and obtain the following truncated SVD:

$$\mathbf{K}^1 \approx \tilde{\mathbf{U}}^1 \tilde{\mathbf{S}}^1 (\tilde{\mathbf{V}}^1)^T.$$

Here $\tilde{\mathbf{S}}^1 = \mathrm{diag}\{\sigma_s\}_{1 \le s \le \tau^1}$ is a $\tau^1 \times \tau^1$ diagonal matrix, $\tilde{\mathbf{U}}^1$ and $\tilde{\mathbf{V}}^1$ are the first τ_1 columns of $\mathbf{U}^1$ and $\mathbf{V}^1$, respectively, and τ_1 is the number of preserved singular values which indicates the numerical rank of $\mathbf{K}^1$. Similar procedures can be executed for the remaining matrices $\mathbf{K}^i$ to obtain their truncated SVDs:

$$\mathbf{K}^i \approx \tilde{\mathbf{U}}^i \tilde{\mathbf{S}}^i (\tilde{\mathbf{V}}^i)^T,$$

where the unitary matrices $\tilde{\mathbf{U}}^i$ and $\tilde{\mathbf{V}}^i$ have the size $M \times \tau_i$ and $\tilde{M} \times \tau_i$ respectively, and the $\tau_i \times \tau_i$ diagonal matrix $\tilde{\mathbf{S}}^i$ consists of the first τ_i singular values, for $i = 2, \cdots, n_z$. Although it is expensive to compute the truncated SVDs of $\mathbf{K}^i$, this computational procedure is executed only once as a preprocessing step and we store those matrices $[\tilde{\mathbf{U}}^i, \tilde{\mathbf{S}}^i, \tilde{\mathbf{V}}^i]$ so that we can reload them whenever they are needed.

Based on these truncated SVDs, we have the following evaluations for formulas (29) and (30):

$$\begin{aligned} \mathbf{P} &= \tilde{h}^3 \cdot [\mathbf{K}^1, \cdots, \mathbf{K}^{n_z}] \chi^T = \tilde{h}^3 \cdot \sum_{i=1}^{n_z} \mathbf{K}^i (\chi_i)^T \\ &\approx \tilde{h}^3 \cdot \sum_{i=1}^{n_z} (\tilde{\mathbf{U}}^i (\tilde{\mathbf{S}}^i (\chi_i \tilde{\mathbf{V}}^i)^T)) \,; \end{aligned} \tag{31}$$

and

$$\mathbf{F}_i = h^2 \cdot \mathbf{d}^T \mathbf{K}^i \mathbf{D}_i \approx h^2 \cdot ((\mathbf{d}^T \tilde{\mathbf{U}}^i) \tilde{\mathbf{S}}^i)(\mathbf{D}_i^T \tilde{\mathbf{V}}^i)^T, \quad 1 \le i \le n_z \tag{32}$$

$$\mathbf{F} = [\mathbf{F}_1, \mathbf{F}_2, \cdots, \mathbf{F}_{n_z}]. \tag{33}$$

In the above, for $1 \le i \le n_z$, we have defined

$$\begin{aligned} \chi_i &= [\chi(\tilde{\mathbf{r}}_1^i), \chi(\tilde{\mathbf{r}}_2^i), \cdots, \chi(\tilde{\mathbf{r}}_{\tilde{M}}^i)] \,, \\ \mathbf{D}_i &= \mathrm{diag}\left\{\mathcal{I}_{T_\epsilon}(\tilde{\mathbf{r}}_l^i)\right\}_{1 \le l \le \tilde{M}} . \end{aligned}$$

Since the diagonal entry $\mathcal{I}_{T_\epsilon}(\tilde{\mathbf{r}}_l^i)$ in $\mathbf{D}_i$ is 0 when $\tilde{\mathbf{r}}_l^i \in \Omega \setminus T_\epsilon$, we perform the multiplication of $\mathbf{D}_i^T$ and $\tilde{\mathbf{V}}^i$ at first to avoid some unnecessary calculations as shown in equation (32).

To sum up, we mention that $\mathcal{O}(\tilde{M}) = \mathcal{O}(M) = \mathcal{O}(N^{2/3})$, therefore by equations (31), (32) and (33), the computational complexity is reduced from $\mathcal{O}(N^{5/3})$ to

$$\sum_{i=1}^{n_z} \mathcal{O}(\tau_i \tilde{M}) = \mathcal{O}(N^{2/3} \sum_{i=1}^{n_z} \tau_i).$$

In practice, according to the accuracy requirement, one can adjust the threshold ϵ_{SVD} to make the sum of τ_i smaller and to further improve the performance of this low-rank-matrix decomposition algorithm.

5 Numerical examples

In this section we provide numerical examples to illustrate the performance of the inversion algorithm. The computational domain is set to be $\Omega = [0,1]\text{km} \times [0,1]\text{km} \times [-0.5,0]\text{km}$, which is uniformly discretized using $41 \times 41 \times 21$ mesh grids. The magnetic anomalous data d^* are collected on the measurement surface $\Gamma = [0,1]\text{km} \times [0,1]\text{km} \times \{z = 0.1\text{km}\}$, and there are $21 \times 21 = 441$ observation points uniformly distributed on Γ. Moreover the regularization weight α in the total objective function E_t is selected in the order of $10^{-3} \cdot \left(\frac{1}{4\pi} B^0 \cdot \chi\right)^2$, and specific values will be given in the examples. In our coordinate system, the x-axis corresponds to the geographic east, the y-axis corresponds to the geographic north, and z-axis coincides with the depth direction.

5.1 Single level-set examples

Firstly we provide some examples of the single level set formulation; that is, there is only one type of magnetic mineral in the subsurface and one level set function ϕ_0 is involved in the inversion algorithm. The initial guess of ϕ_0 takes the following form

$$\phi_{0,\text{initial}} = 1 - \sqrt{\frac{(x-0.5)^2}{0.4^2} + \frac{(y-0.5)^2}{0.4^2} + \frac{(z+0.25)^2}{0.2^2}},$$

which is approximately a signed distance function to an ellipsoid.

5.1.1 Two dykes

The model consists of two 3-D dykes buried in a non-susceptible half-space. Figure 1 (a) shows the exact model, where the susceptibility value χ_0 is given to be $\chi_0 = 0.04$. Under an inducing field with a strength of $B^0 = 5 \times 10^4\,\text{nT}$ and a direction at inclination $I = 75^0$ and declination $D = 25^0$, the magnetic anomalous data are collected on the measurement

surface $\Gamma = \{z = 0.1\text{km}\}$ as shown in Figure 1 (b). Figure 1 (c) displays the initial guess of the underlying structure in our inversion algorithm.

We set the regularization weight $\alpha = 25$ in this example, which is in the order of $10^{-3} \cdot \left(\frac{1}{4\pi} B^0 \cdot \chi_0\right)^2$. Figure 1 (d) provides the recovered structure after 3000 iterations. The single ellipsoid in the initial guess is separated into two disconnecting source bodies, and the locations of two dykes are well captured. In Figure 1 (e) and Figure 1 (f) we also plot the cross-sections of the structure at $x = 0.5$km and $z = -0.15$km respectively, where the dashed line indicates the exact model and the solid line plots the recovered structure. In these figures the inversion solution matches well with the exact model, where the shape and depth of two dykes are successfully recovered, though the solution loses sharp corners of the exact model due to regularization introduced in our inversion algorithm.

To further test the robustness of the algorithm, we have perturbed the measured magnetic data d^* by 5% Gaussian noise with zero mean and repeated the inversion process. The results are shown in Figure 2, where Figure 2 (a) shows the measured data with 5% Gaussian noise, Figure 2 (b) provides the solution after 3000 iterations, Figure 2 (c) plots the cross-section at $x = 0.5$km and Figure 2 (d) shows the cross-section at $z = -0.15$km. Since the solution is similar to the recovered solution using the clean measurements as shown in Figure 1, our inversion algorithm is not sensitive to noise.

5.1.2 Four source bodies

In this example, the model consists of two spheres and two cuboids buried in varying depths. Figure 3 (a) shows the exact model, where the susceptibility value χ_0 is given to be $\chi_0 = 0.04$. The primary inducing field is in the direction of $I = 90^0$ with a strength of $B^0 = 5 \times 10^4$ nT, and the magnetic anomaly data are collected on the measurement surface $\Gamma = \{z = 0.1\text{km}\}$ as shown in Figure 3 (b). Figure 3 (c) displays the initial guess of the underlying structure which is the same as the initialization in the two-dyke example. The regularization weight α is again set to be $\alpha = 25$ in the total objective function. Figure 3 (d) provides the solution after 5000 iterations, where the single ellipsoid in the initial guess evolves into four objects, and the shapes and locations of all source bodies are successfully recovered.

To display the results more clearly we also provide the pictures of cross-sections in Figure 4. Cross-sections of the underlying structure are displayed at $x = 0.25$km, $x = 0.75$km, $z = -0.2$km, $z = -0.3$km, and $z = -0.4$km, respectively, where the dashed line indicates the exact structure and the solid line plots the recovered solution. The reconstruction matches well with the exact model, and our level set algorithm can automatically generate separated source bodies with varying depths to fit the given data.

5.2 Multiple level-set examples

In this subsection we provide examples of multiple level set formulations; that is, there are two types of magnetic minerals in the underlying subsurface and two level set functions ϕ_1

and ϕ_2 are introduced in the inversion algorithm. Unless otherwise specified, we set the initial guess of ϕ_1 to be

$$\phi_{1,\text{initial}} = 1 - \sqrt{\frac{(x-0.75)^2}{0.15^2} + \frac{(y-0.5)^2}{0.4^2} + \frac{(z+0.25)^2}{0.2^2}} \tag{34}$$

and the initial guess of ϕ_2 to be

$$\phi_{2,\text{initial}} = 1 - \sqrt{\frac{(x-0.25)^2}{0.15^2} + \frac{(y-0.5)^2}{0.4^2} + \frac{(z+0.25)^2}{0.2^2}}, \tag{35}$$

so that the shape of the initial structure consists of two ellipsoids.

5.2.1 Three source bodies with different susceptibilities

As shown in Figure 5 (a), the exact model consists of three cuboids with different susceptibilities $\chi_1 = 0.04$ and $\chi_2 = 0.08$, where the gray color indicates the object with lower susceptibility $\chi_1 = 0.04$ and the dark color indicates the source bodies with higher susceptibility $\chi_2 = 0.08$. Figure 5(b) shows the magnetic data collected on the measurement surface $\Gamma = \{z = 0.1\text{km}\}$, which is generated under an inducing field with a strength of $B^0 = 5 \times 10^4\,\text{nT}$ and a direction at the inclination $I = 90^0$. As we can see, the intensity of magnetic data varies a lot on the measurement surface. We are trying to recover this model using our multiple level set algorithm.

The initial guess is displayed in Figure 5(c), where the gray color indicates $\chi_1 = 0.04$ and the dark color indicates $\chi_2 = 0.08$. We choose the regularization weight $\alpha = 50$ in this example, which is in the order of $10^{-3} \times \left(\frac{1}{4\pi} B^0 \chi_2\right)^2$. Figure 5 (d) shows the result after 3000 iterations, where the recovered solution successfully captures the shapes and locations of the underlying source bodies. To display the result more clearly we also plot the cross-sections in Figure 6, where we provide slices of the structure at $x = 0.2$km, $x = 0.7$km, $z = -0.25$km, and $z = -0.35$km, respectively. Again the dashed line indicates the exact model and the solid line plots the recovered structure, and the gray color corresponds to $\chi_1 = 0.04$ and the dark color corresponds to $\chi_2 = 0.08$. Figure 6 (a) and Figure 6 (b) show that the varying depths of different source bodies are well located. Figure 6 (c) and Figure 6 (d) show that the recovered structure coincides with the exact model in shape.

To further test robustness of our multiple level set algorithm we repeat the inversion process by adding 5% Gaussian noise with zero mean to the measurement data d^*, and we provide the result in Figure 7. Figure 7 (a) shows the measured magnetic data perturbed by 5% Gaussian noise. Figure 7 (b) provides the solution after 3000 iterations. Figures 7 (c)-7 (f) display the cross-sections of the structure at $x = 0.2$km, $x = 0.7$km, $z = -0.25$km, and $z = -0.35$km, respectively. We conclude that the result is quite similar to the recovered solution using the clean measurements as shown in Figure 5 and Figure 6, and the multiple level set algorithm is not sensitive to noise.

5.2.2 Four source bodies with different susceptibilities

In this example the exact model is shown in Figure 8 (a), where the dark sphere and the dark dyke have the same susceptibility $\chi_2 = 0.08$, and the gray cuboids have susceptibility $\chi_1 = 0.04$. Under an inducing field with a strength of 5×10^4 nT and a direction at $I = 75^0$ and $D = 25^0$, the magnetic anomaly data are collected on the measurement surface $\Gamma = \{z = 0.1\text{km}\}$ as shown in Figure 8 (b). Figure 8 (c) shows the initial guess which is the same as the initialization of the three-source-body example. Again the regularization weight in the total objective function is set to be $\alpha = 50$. We perform the multiple level set algorithm to invert for the underlying structure, and we provide the solution after 2000 iterations in Figure 8 (d). Four separate source bodies are recovered, where the gray color indicates $\chi_1 = 0.04$ and the dark color indicates $\chi_2 = 0.08$. From the 3-D visualization one can find that the locations of different source bodies are well recovered. To display the shape of structure more clearly we also plot the cross-sections in Figure 9, where we display the slices at $x = 0.75$km, $y = 0.8$km, $y = 0.375$km, $z = -0.15$km, and $z = -0.3$km, respectively. Again the dashed line indicates the exact model and the solid line plots the recovered solution; the gray color corresponds to $\chi_1 = 0.04$ and the dark color corresponds to $\chi_2 = 0.08$. Our solution is reasonable and the recovered structure gives helpful information of the underlying source bodies, though there are some distortions due to the complexity of the underlying structure. For example, in Figure 9 (a), the recovered structure near $\{x = 0.75\text{km},\ y = 0.6\text{km}\}$ is shallower than the exact source body, and this is partly because the magnetic anomaly data generated by the deeply buried source body is not significant comparing to its ambient data, where one can refer to Figure 8 (b) for the shape of measurement data.

5.3 Inherent non-uniqueness with two types of primary minerals

We illustrate the limitation of our multiple level set algorithm. The exact model is shown in Figure 10(a), where two dykes are buried in the south-north and north-south directions both with a dipping angle of 45^0, and the gray color indicates the source body with lower susceptibility $\chi_1 = 0.04$ and the dark color indicates the higher susceptibility $\chi_2 = 0.08$. Under an inducing field with a strength of 5×10^4 nT and a direction at $I = 75^0$ and $D = 25^0$, the magnetic anomaly data is collected on the measurement surface $\Gamma = \{z = 0.1\text{km}\}$ as shown in Figure 10 (b). We set the regularization weight in the total objective function to be $\alpha = 50$, and we perform inversion twice with different sets of initial guesses.

In the first experiment the initial guess of $\phi_i\,(i = 1, 2)$ is shown in equations (34) and (35) and displayed in Figure 11 (a). Figure 11 (b) gives the recovered solution after 2000 iterations, and Figures 11 (c)-11 (f) display the cross-sections at $x = 0.3$km, $x = 0.7$km, $z = -0.15$km, and $z = -0.25$km, respectively. The recovered structure matches well with the exact model so that the shapes and locations of two different dykes are well recovered.

In the second experiment we interchange the initializations of ϕ_1 and ϕ_2 so that

$$\phi_{1,\text{initial}} = 1 - \sqrt{\frac{(x-0.25)^2}{0.15^2} + \frac{(y-0.5)^2}{0.4^2} + \frac{(z+0.25)^2}{0.2^2}},$$

$$\phi_{2,\text{initial}} = 1 - \sqrt{\frac{(x-0.75)^2}{0.15^2} + \frac{(y-0.5)^2}{0.4^2} + \frac{(z+0.25)^2}{0.2^2}}.$$

Figure 12 (a) displays the shape of initial guess, where the gray color indicates $\chi_1 = 0.04$ and the dark color indicates $\chi_2 = 0.08$. Figure 12 (b) provides the recovered solution, and Figures 12 (c)-12 (f) display the cross-sections at $x = 0.3$km, $x = 0.7$km, $z = -0.15$km, and $z = -0.25$km, respectively. One finds that the recovered solution is different from the exact model as shown in Figure 10 (a); essentially the positions of two dykes with different susceptibilities are interchanged in the recovered structure. The gray dyke with susceptibility $\chi_1 = 0.04$ is replaced by a smaller source body with higher susceptibility $\chi_2 = 0.08$, and the dark dyke with susceptibility $\chi_2 = 0.08$ is replaced by a larger source body with lower susceptibility $\chi_1 = 0.04$.

We mention that this effect is due to the inherent non-uniqueness in the magnetic inversion problem. In this example the structures in Figures 11 (b) and 12 (b) have generated similar magnetic anomaly data on the measurement surface $\Gamma = \{z = 0.1\text{km}\}$ so that either of them can fit the data generated by the underlying structure. We may need more information of the magnetic mass distributions in the underlying subsurface so that we can choose an appropriate initial guess to recover the expected solution.

6 Conclusion

In this paper we have proposed a level set method for 3-D inversion of magnetic data. We have applied a single level set formulation for the model with one type of primary mineral in the subsurface, and a multiple level set formulation for the model with two types of magnetic minerals. With the knowledge of the types of underlying minerals and the values of magnetic susceptibilities, the level set algorithm takes full advantage of a priori information and it alleviates the inherent non-uniqueness in the magnetic inversion problem. The methodology can be generalized to a subsurface structure with arbitrarily many types of magnetic minerals; however, the inherent non-uniqueness in the magnetic inversion problem prevents us to do so for more than two types of primary minerals. We have provided plentiful numerical examples, which illustrate the effectiveness and also the limitation of the proposed algorithm.

Acknowledgments

Qian is supported by NSF-1222368.

References

[1] M. K. Ben Hadj Miled and E. L. Miller. A projection-based level-set approach to enhance conductivity anomaly reconstruction in electrical resistance tomography. *Inverse Problem*, 23:2375–2400, 2007.

[2] B. K. Bhattacharyya. A generalized multibody model for inversion of magnetic anomalies. *Geophysics*, 45(2):255–270, 1980.

[3] R. N. Bracewell. *The Fourier Transform and Its Applications*. Electrical engineering series. McGraw Hill, 2000.

[4] M. Burger and S. Osher. A survey on level set methods for inverse problems and optimal design. *European J. Appl. Math.*, 16:263–301, 2005.

[5] T. Cecil, S. J. Osher, and J. Qian. Simplex free adaptive tree fast sweeping and evolution methods for solving level set equations in arbitrary dimension. *J. Comput. Phys.*, 213:458–473, 2006.

[6] F. Cella and M. Fedi. Inversion of potential field data using the structural index as weighting function rate decay. *Geophysical Prospecting*, 60:313–336, 2012.

[7] E. T. Chung, X-C Tai, and T. Chan. Electrical impedance tomography using level set representation and total variational regularization. *J. Comput. Phys.*, 205:357–372, 2005.

[8] A. DeCezaro, A. Leitao, and X-C Tai. On multiple level-set regularization methods for inverse problems. *Inverse Problems*, 25(3):035004, 2009.

[9] O. Dorn and D. Lesselier. Level set methods for inverse scattering. *Inverse Problems*, 22:R67–R131, 2006.

[10] M. Fedi and M. Pilkington. Understanding imaging methods for potential field data. *Geophysics*, 77:G13–G24, 2012.

[11] S. Hou, K. Solna, and H.-K. Zhao. Imaging of location and geometry for extended targets using the response matrix. *J. Comput. Phys.*, 199:317–338, 2004.

[12] V. Isakov. *Inverse source problems*. American Mathematical Society, Providence, Rhode Island, 1990.

[13] V. Isakov, S. Leung, and J. Qian. A fast local level set method for inverse gravimetry. *Comm. in Computational Physics*, 10:1044–1070, 2011.

[14] V. Isakov, S. Leung, and J. Qian. A three-dimensional inverse gravimetry problem for ice with snow caps. *Inverse Problems and Imaging*, 7:523–544, 2013.

[15] P. Lelièvre and D. Oldenburg. Magnetic forward modelling and inversion for high susceptibility. *Geophysical Journal International*, 166(1):76–90, 2006.

[16] Peter G. Lelièvre. Forward modeling and inversion of geophysical magnetic data. Master's thesis, University of British Columbia, Canada, 2003.

[17] S. Leung, J. Qian, and R. Burridge. Eulerian Gaussian beams for high frequency wave propagation. *Geophysics*, 72:SM61–SM76, 2007.

[18] S. Leung, J. Qian, and S. J. Osher. A level set method for three dimensional paraxial geometrical optics with multiple sources. *Comm. Math. Sci.*, 2:657–686, 2004.

[19] W. Li and S. Leung. A fast local level set based adjoint state method for first arrival transmission travletime tomography with discontinuous slowness. *Geophysical Journal International*, 195:582–596, 2013.

[20] W. Li, S. Leung, and J. Qian. A level set-adjoint state method for crosswell transmission-reflection traveltime tomography. *Geophys. J. Internat.*, 199:348–367, 2015.

[21] Y. Li and D. Oldenburg. 3-D inversion of magnetic data. *Geophysics*, 61(2):394–408, 1996.

[22] Y. Li and D. Oldenburg. 3D inversion of gravity data. *Geophysics*, 63:109–119, 1998.

[23] A. Litman, D. Lesselier, and F. Santosa. Reconstruction of a 2-D binary obstacle by controlled evolution of a level-set. *Inverse Problems*, 14:685–706, 1998.

[24] W. Lu, S. Leung, and J. Qian. An improved fast local level set method for three-dimensional inverse gravimetry. *Inverse Problems and Imaging*, 9:479–509, 2015.

[25] W. Lu and J. Qian. A local level set method for three-dimensional inversion of gravity gradiometry data. *Geophysics*, 80:G35–G51, 2015.

[26] S. J. Osher and J. A. Sethian. Fronts propagating with curvature dependent speed: algorithms based on Hamilton-Jacobi formulations. *J. Comput. Phys.*, 79:12–49, 1988.

[27] D. Papadopoulos, M. Herty, V. Rath, and M. Behr. Identification of uncertainties in the shape of geophysical objects with level sets and the adjoint method. *Computational Geosciences*, 15:737–753, 2011.

[28] O. Portniaguine and M. S. Zhdanov. 3-D magnetic inversion with data compression and image focusing. *Geophysics*, 67(5):1532–1541, 2002.

[29] J. Qian, L.-T. Cheng, and S. J. Osher. A level set based Eulerian approach for anisotropic wave propagations. *Wave Motion*, 37:365–379, 2003.

[30] J. Qian and S. Leung. A level set method for paraxial multivalued traveltimes. *J. Comput. Phys.*, 197:711–736, 2004.

[31] J. Qian and S. Leung. A local level set method for paraxial multivalued geometric optics. *SIAM J. Sci. Comp.*, 28:206–223, 2006.

[32] J. Qian and W. W. Symes. An adaptive finite difference method for traveltime and amplitude. *Geophysics*, 67:167–176, 2002.

[33] J. Qian and W. W. Symes. Finite-difference quasi-P traveltimes for anisotropic media. *Geophysics*, 67:147–155, 2002.

[34] F. Santosa. A level-set approach for inverse problems involving obstacles. *Control, Optimizat. Calculus Variat.*, 1:17–33, 1996.

[35] M. Sussman, P. Smereka, and S. J. Osher. A level set approach for computing solutions to incompressible two-phase flows. *J. Comput. Phys.*, 114:146–159, 1994.

[36] X-C Tai and T. Chan. A survey on multiple level set methods with applications for identifying piecewise constant functions. *Inter. J. Numer. Anal. Model*, 1(1):25–47, 2004.

[37] K. van den Doel, U. Ascher, and A. Leitao. Multiple level sets for piecewise constant surface reconstruction in highly ill-posed problems. *J. Sci. Comput.*, 43:44–66, 2010.

[38] X. Wang and R. O. Hansen. Inversion for magnetic anomalies of arbitrary three-dimensional bodies. *Geophysics*, 55(10):1321–1326, 1990.

[39] H.-K. Zhao, T. Chan, B. Merriman, and S. J. Osher. A variational level set approach for multiphase motion. *J. Comput. Phys.*, 127:179–195, 1996.

[40] M. Zhdanov. *Geophysical inverse theory and regularization problems*, volume 36. Elsevier, 2002.

[41] P. Zheglova, C. G. Farquharson, and C. A. Hurich. 2-D reconstruction of boundaries with level set inversion of traveltiems. *Geophysical Journal International*, 192:688–698, 2013.

List of Figures

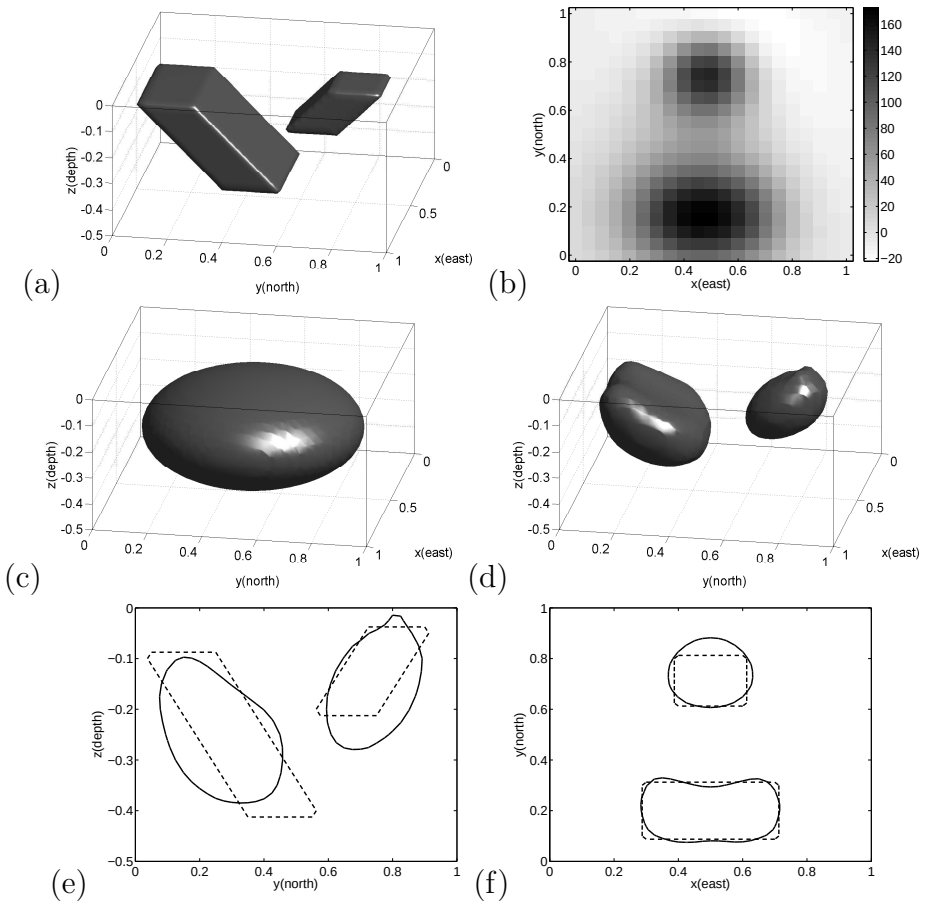

Figure 1: Two dykes. (a) exact model; (b) magnetic anomaly data collected on the measurement surface; (c) initial guess; (d) solution after 3000 iterations; (e) cross-section at $x = 0.5$km; (f) cross-section at $z = -0.15$km.

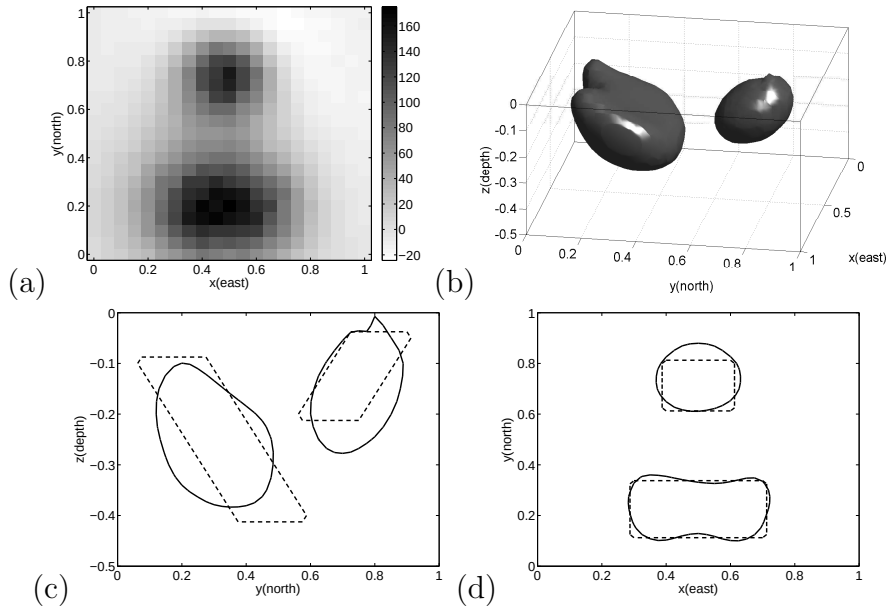

Figure 2: Two dykes with 5% Gaussian noise added to the measurement. (a) magnetic anomaly data with 5% Gaussian noise; (b) solution after 3000 iterations; (c) cross-section at $x = 0.5$km; (d) cross-section at $z = -0.15$km.

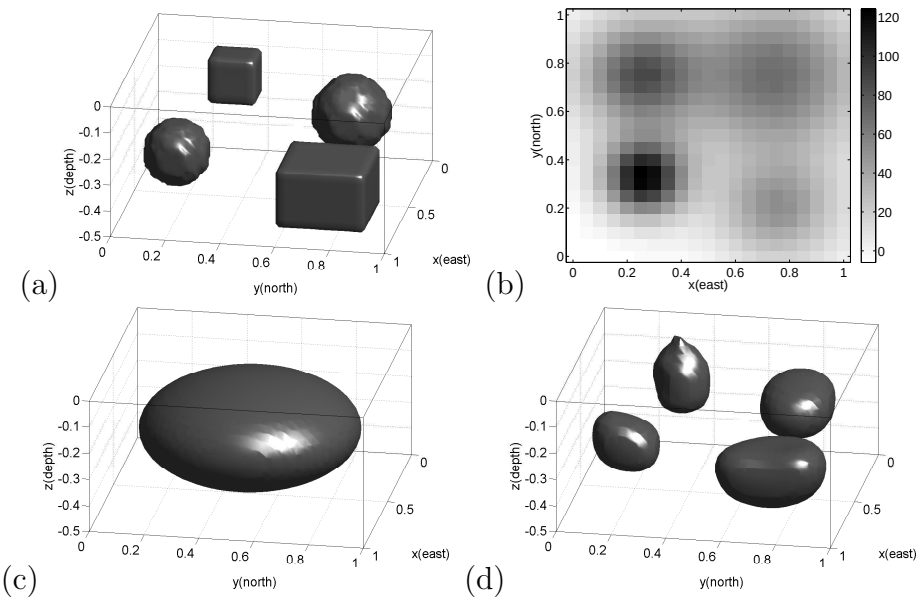

Figure 3: Four source bodies. (a) exact model; (b) magnetic anomaly data collected on the measurement surface; (c) initial guess; (d) solution after 5000 iterations.

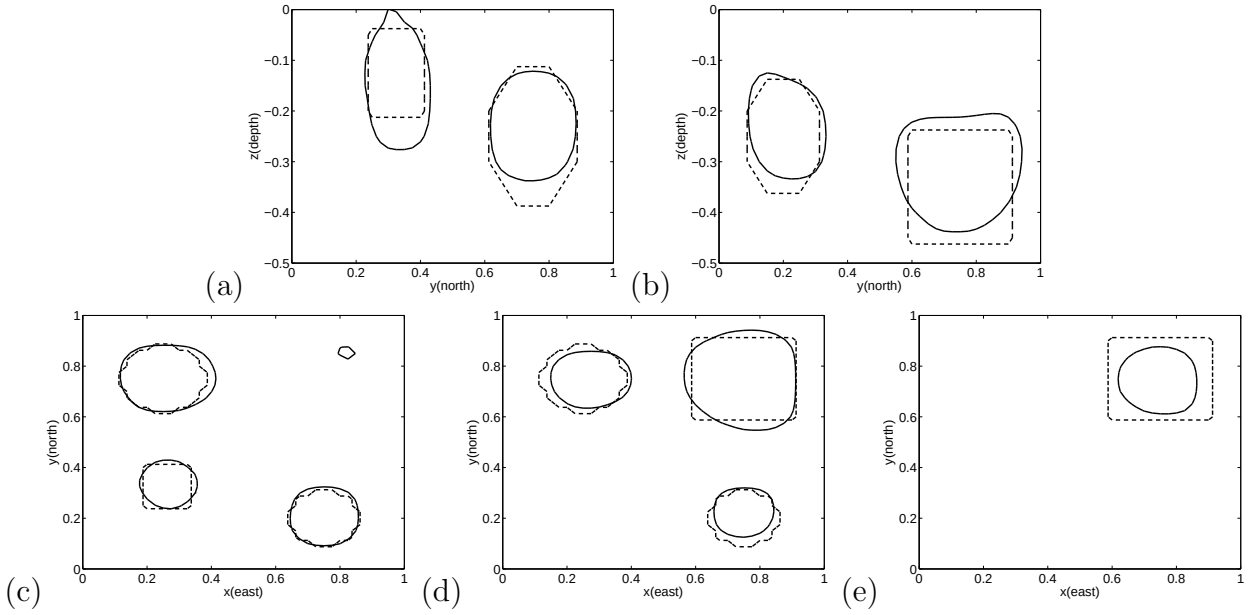

Figure 4: Four source bodies. Display of cross-sections. The dashed line indicates the exact model, and the solid line plots the recovered structure. (a) $x = 0.25$km; (b) $x = 0.75$km; (c) $z = -0.2$km; (d) $z = -0.3$km; (e) $z = -0.4$km

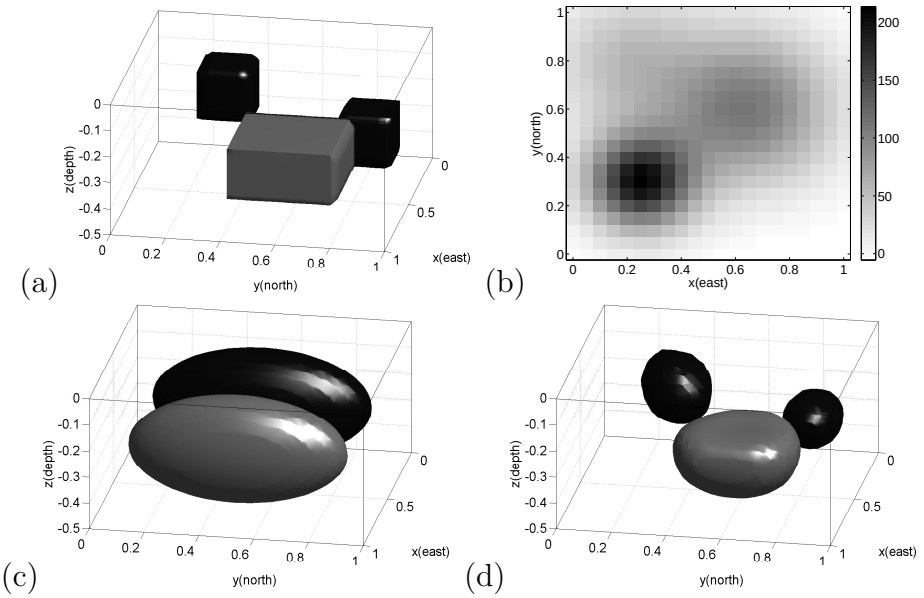

Figure 5: Three source bodies with different susceptibilities. (a) exact model; (b) magnetic anomaly data collected on the measurement surface; (c) initial guess; (d) solution after 3000 iterations. The gray color indicates $\chi_1 = 0.04$ and the dark color indicates $\chi_2 = 0.08$.

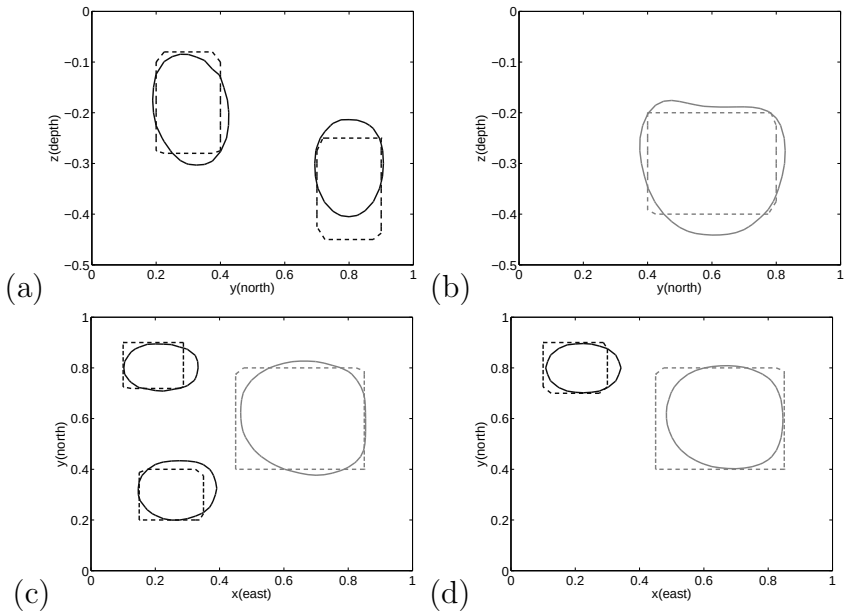

Figure 6: Three source bodies with different susceptibilities, display of cross-sections. The dashed line indicates the exact model, the solid line plots the recovered structure; the gray color corresponds to $\chi_1 = 0.04$ and the dark color corresponds to $\chi_2 = 0.08$. (a) $x = 0.2$km; (b) $x = 0.7$km; (c) $z = -0.25$km; (d) $z = -0.35$km

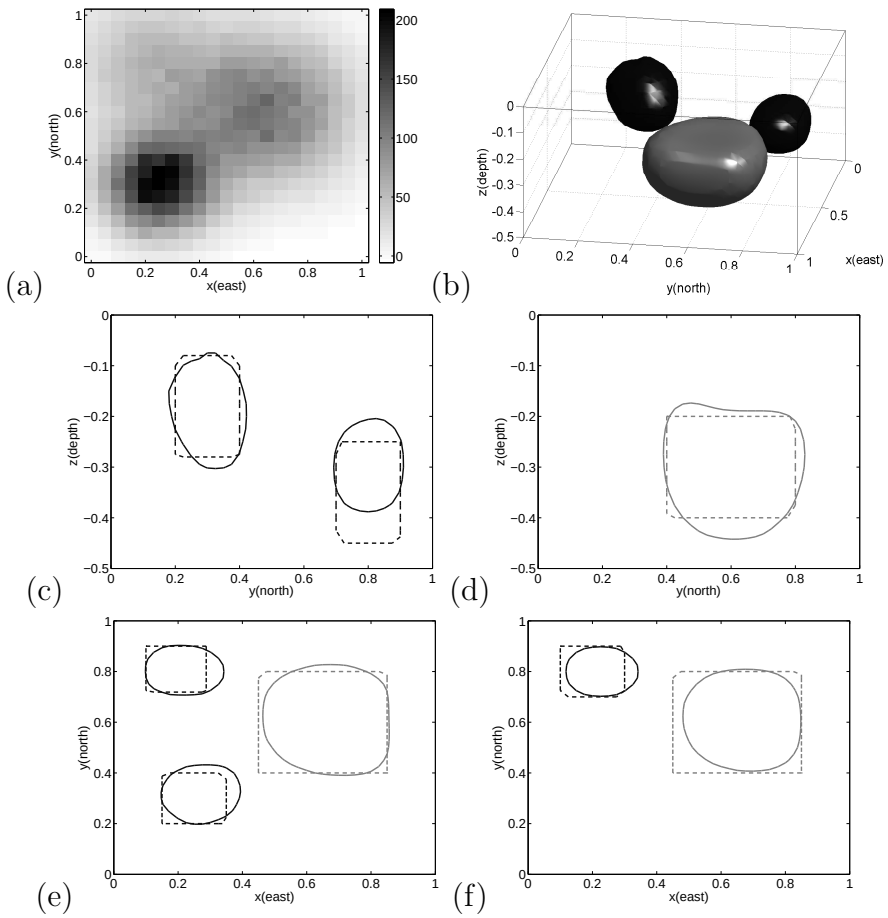

Figure 7: Three source bodies with different susceptibilities, 5% Gaussian noise added to the measurement. (a) magnetic anomaly data with 5% Gaussian noise; (b) solution after 3000 iterations; (c)-(f) cross-sections at $x = 0.2$km, $x = 0.7$km, $z = -0.25$km, and $z = -0.35$km, respectively. The dashed line indicates the exact model and the solid line plots the recovered structure; the gray color corresponds to $\chi_1 = 0.04$ and the dark color corresponds to $\chi_2 = 0.08$.

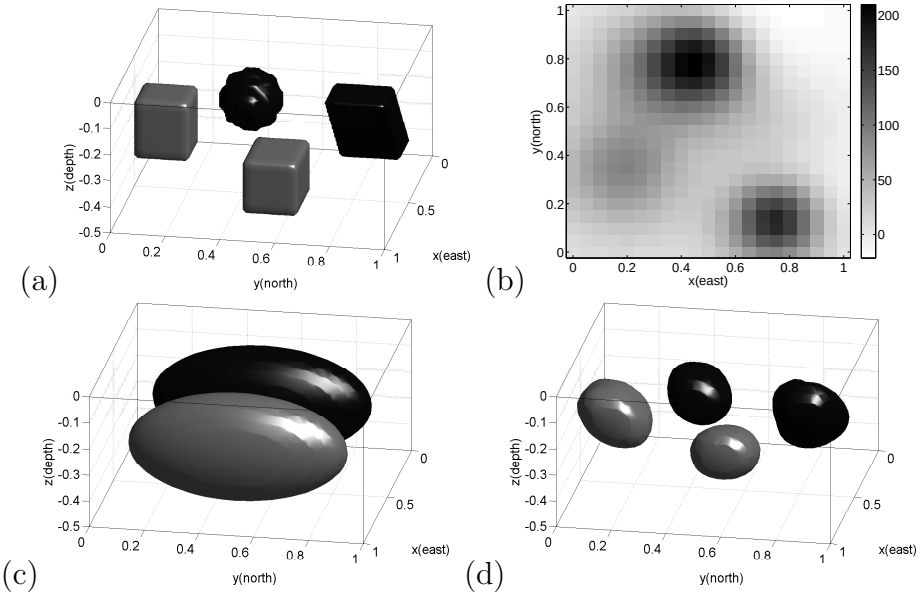

Figure 8: Four source bodies with different susceptibilities. (a) exact model; (b) magnetic anomaly data collected on the measurement surface; (c) initial guess; (d) solution after 2000 iterations. The gray color indicates $\chi_1 = 0.04$ and the dark color indicates $\chi_2 = 0.08$.

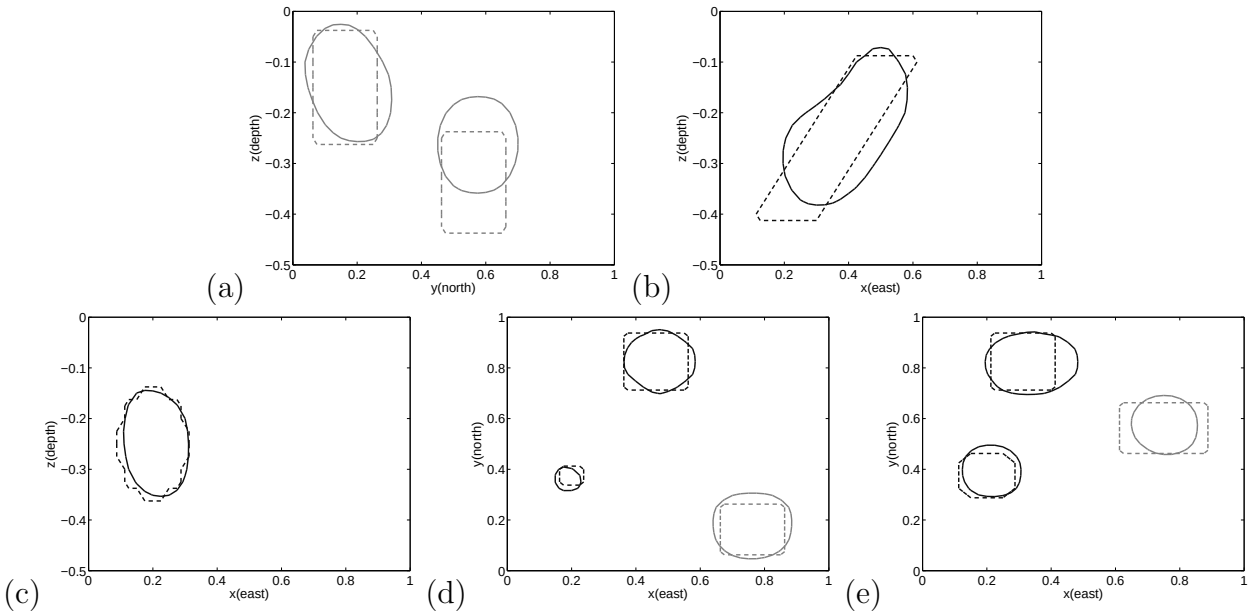

Figure 9: Four source bodies with different susceptibilities, display of cross-sections. The dashed line indicates the exact model, the solid line plots the recovered structure; the gray color corresponds to $\chi_1 = 0.04$ and the dark color corresponds to $\chi_2 = 0.08$. (a) $x = 0.75$km; (b) $y = 0.8$km; (c) $y = 0.375$km; (d) $z = -0.15$km; (e) $z = -0.3$km

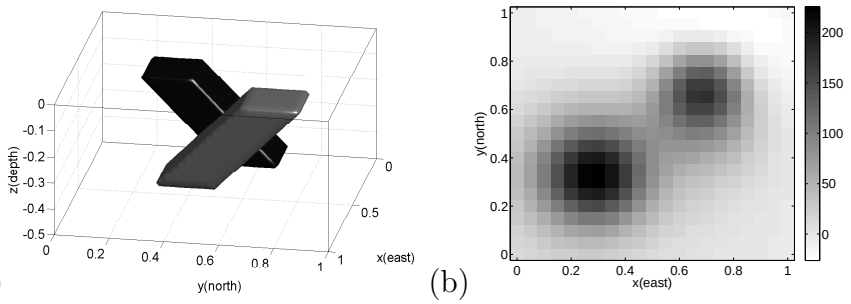

Figure 10: Inherent non-uniqueness. (a) Exact model. (b) magnetic anomaly data. In (a) the gray color indicates $\chi_1 = 0.04$ and the dark color indicates $\chi_2 = 0.08$.

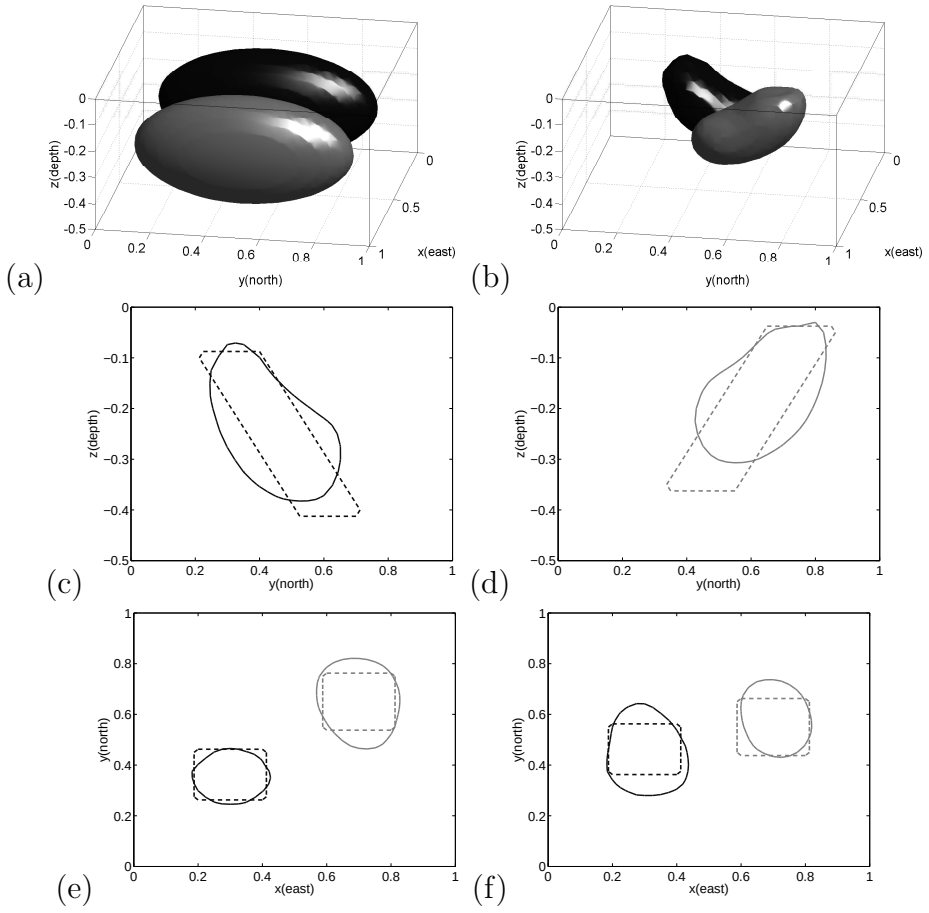

Figure 11: Inherent non-uniqueness, solution using the first set of initial guess. (a) Initial guess; (b) solution after 2000 iterations; (c)-(f) cross-sections at $x = 0.3$km, $x = 0.7$km, $z = -0.15$km and $z = -0.25$km, respectively. The dashed line indicates the exact model, the solid line plots the recovered structure; the gray color corresponds to $\chi_1 = 0.04$ and the dark color corresponds to $\chi_2 = 0.08$.

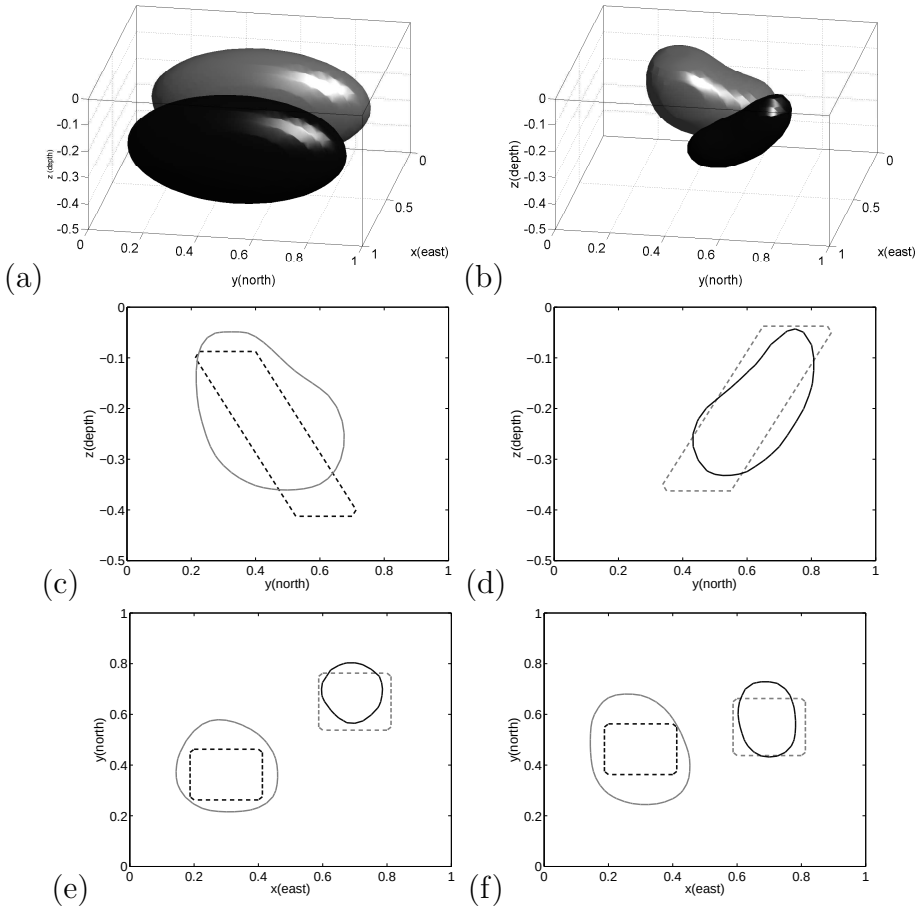

Figure 12: Inherent non-uniqueness, solution using the second set of initial guess. (a) Initial guess; (b) solution after 2000 iterations; (c)-(f) cross-sections at $x = 0.3$km, $x = 0.7$km, $z = -0.15$km and $z = -0.25$km, respectively. The dashed line indicates the exact model, the solid line plots the recovered structure; the gray color corresponds to $\chi_1 = 0.04$ and the dark color corresponds to $\chi_2 = 0.08$.